Density dependence of the symmetry energy in the post–PREX-CREX era

Brendan T. Reed [1,2,*] F. J. Fattoyev [3,†] C. J. Horowitz [4,5,‡] and J. Piekarewicz [6,§]

[1]*Theoretical Division, Los Alamos National Laboratory, Los Alamos, New Mexico 87545, USA*
[2]*Department of Astronomy, Indiana University, Bloomington, Indiana 47405, USA*
[3]*Department of Physics & Astronomy, Manhattan College, Riverdale, New York 10471, USA*
[4]*Facility for Rare Isotope Beams, Michigan State University, East Lansing, Michigan 48824, USA*
[5]*Center for Exploration of Energy and Matter and Department of Physics, Indiana University, Bloomington, Indiana 47405, USA*
[6]*Department of Physics, Florida State University, Tallahassee, Florida 32306, USA*

The recently published CREX results suggest a rather peculiar picture for the density dependence of the symmetry energy. Whereas PREX favors a large neutron skin thickness in ^{208}Pb, thereby suggesting a stiff equation of state, CREX suggests instead a much softer equation of state. This discrepancy has caused a large spur in the theoretical community, since no model has been able to simultaneously reproduce within 1σ the PREX and CREX results. Motivated by a novel correlation between a CREX observable and a combination of bulk symmetry energy parameters, we calibrate three new covariant energy density functionals that reproduce binding energies and charge radii of spherical nuclei—and also accommodate the constraints imposed by PREX and CREX. Given that these models suggest a stiff equation of state at high densities, predictions for neutron star properties are also discussed.

I. INTRODUCTION

After almost a decade since first conceived, the Calcium Radius Experiment (CREX) at Thomas Jefferson National Accelerator Facility (JLab) was recently completed [1]. CREX followed on the footsteps of the successful Lead Radius Experiment (PREX) [2–4] that aimed to constrain the equation of state (EOS) of neutron star matter in the vicinity of nuclear saturation density by measuring the neutron skin thickness of ^{208}Pb. Such a powerful connection between atomic nuclei and neutron stars is encoded in the nuclear symmetry energy, which quantifies the energy cost of converting symmetric nuclear matter into pure neutron matter. In the vicinity of nuclear saturation density, $\rho_0 \approx 0.15\,\text{fm}^{-3}$, the density dependence of the symmetry energy is parameterized in terms of a few bulk parameters,

$$S(\rho) = J + Lx + \frac{1}{2}K_{\text{sym}}x^2 + \cdots, \quad x \equiv \frac{\rho - \rho_0}{3\rho_0}, \quad (1)$$

where J is the value, L the slope, and K_{sym} the curvature of the symmetry energy at saturation density. In particular, the correlation between the neutron skin thickness of ^{208}Pb and the radius of a canonical $1.4M_\odot$ neutron star indicates that L controls both the thickness of the neutron skin [5–7] and the radius of low-mass neutron stars [8–11].

With tiny parity-violating asymmetries of the order of parts per million [1,4], both CREX and PREX-2 determined the neutral weak form factors F_{wk} of ^{48}Ca and ^{208}Pb at a single value of the momentum transfer. These values are as model independent as the ones extracted decades ago for the corresponding charge form factors F_{ch} using elastic electron scattering [12]. By then exploiting the correlation between the neutron skin thickness $R_{\text{skin}} = R_n - R_p$ and the weak skin form factor $F_{\text{Wskin}} = F_{\text{ch}} - F_{\text{wk}}$ [13] predicted by several relativistic and nonrelativistic models, a constraint on the neutron skin is obtained. Whereas the theoretical model error is small in the case of ^{208}Pb (about 15% relative to the experimental error), the theoretical and experimental errors are comparable for ^{48}Ca. Thus, in comparing against experiment it is better to use the model-independent CREX weak skin form factor rather than the neutron skin. Although part of the larger theoretical error in ^{48}Ca is associated to the slightly larger-than-optimal experimental momentum transfer, ^{48}Ca presents additional theoretical challenges relative to ^{208}Pb. For example, the tensor component of the current—often referred to as the spin-orbit contribution—becomes important in ^{48}Ca because in a mean-field approximation the $f_{7/2}$ orbital is full while its $f_{5/2}$ spin-orbit partner is empty [14]. Hence, unlike PREX, the connection between CREX and the density dependence of the symmetry energy is not as robust [15].

While some differences between PREX and CREX were anticipated, it came as a surprise to many when CREX reported a central value for the neutron skin thickness of ^{48}Ca (R_{skin}^{48}) that was significantly smaller than the corresponding value for ^{208}Pb (R_{skin}^{208}). Although the correlation between R_{skin}^{48}

*breed@lanl.gov
†ffattoyev01@manhattan.edu
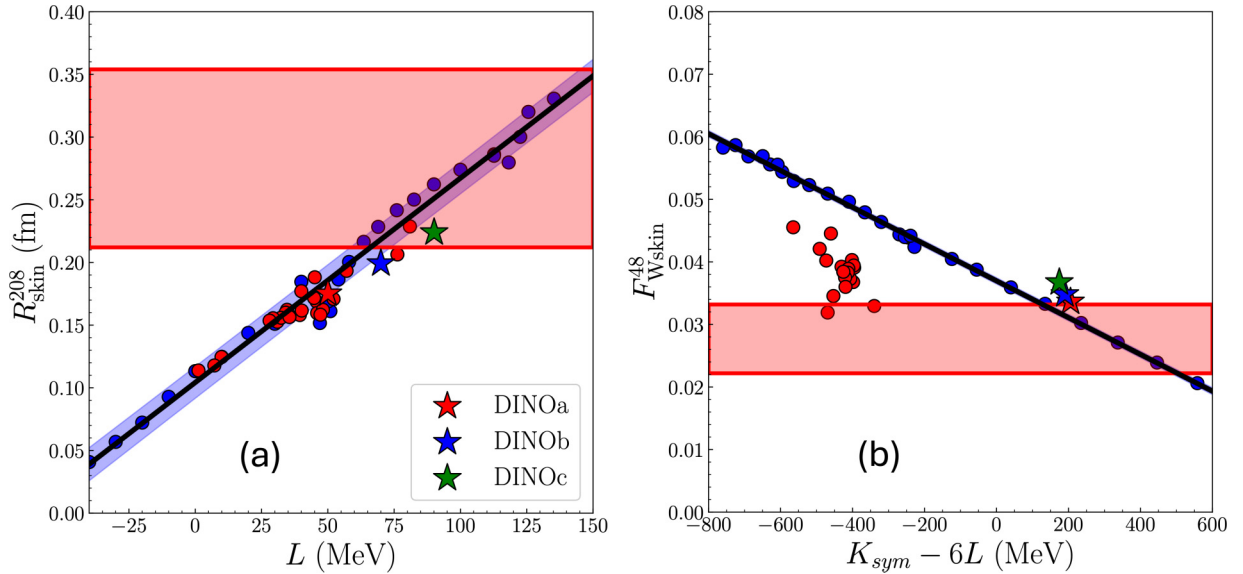‡horowit@indiana.edu
§jpiekarewicz@fsu.edu

FIG. 1. (a) Model predictions for the neutron skin thickness of ^{208}Pb as a function of L and (b) for the weak skin form factor of ^{48}Ca as a function of the linear combination $K_{\mathrm{sym}} - 6L$. The blue and red dots represent the entire set of both covariant and nonrelativistic EDFs used in the CREX analysis [1]. The new DINOa-c interactions are shown as stars. The experimental values are shown as horizontal bands, and the 1σ errors bands for the covariant EDFs are displayed as solid lines with blue bands.

and R_{skin}^{208} may not be as strong as that observed between ^{208}Pb and other heavier neutron-rich nuclei [16], it is difficult to find a theoretical model that can reproduce both. Indeed, several theoretical approaches have attempted unsuccessfully to reconcile both measurements [17–22]. The common theme that has emerged from these studies suggests that it is difficult to accommodate within 1σ the large value of R_{skin}^{208} within the constraints imposed from other nuclear observables, particularly the electric dipole polarizability α_D. Reference [18] goes as far as suggesting that the large error bars reported by the PREX Collaboration makes it difficult to use the parity-violating asymmetry in ^{208}Pb as a meaningful constraint on the isovector sector of current energy density functionals. Finally, a recent *ab initio* approach using chiral forces predicted a value for R_{skin}^{208} that is in mild tension with PREX [17] and for which the correlation between R_{skin}^{208} and R_{skin}^{48} remains fairly strong. Additionally, the range of parameter space inferred by *ab initio* calculations points to the large neutron skin of ^{208}Pb being unlikely [23]. We note that within the *ab initio* framework, a prediction of the neutron skin thickness of ^{48}Ca was made well in advance of the experiment [24] that is entirely consistent with the value reported by the CREX Collaboration. It is the goal of this work to explore refinements to the isovector sector of covariant energy density functionals in an attempt to reconcile the PREX-2 and CREX results. We first begin by showing the correlation of several energy density functional (EDF) predictions of isovector skins with some of the terms of the symmetry energy in Sec. II. We then extract constraints on these terms inferred from the results of both PREX and CREX using a Markov chain Monte Carlo (MCMC) approach in Sec. III. Next, in Sec. IV we generate three new relativistic EDFs that are consistent with the results extracted above. By using these three new EDFs we predict

several properties of nuclear and neutron star matter (see Sec. V). We then conclude in Sec. VI.

II. ISOVECTOR SKIN CORRELATIONS

In a previous article we invoked the strong correlation between R_{skin}^{208} and L to conclude that the symmetry energy is stiff [25]. While it may be possible to soften the symmetry energy by incorporating the CREX results, such an approach seems unnatural given that several recent studies have concluded that the current picture of density functional theory is insufficient to explain why ^{208}Pb has a thick skin and ^{48}Ca has a thin skin [18,22,26]. What may hold the key to elucidate the source of the discrepancy are the higher-order terms in the density expansion of the symmetry energy displayed in Eq. (1), particularly K_{sym}. In what follows we actually argue that the CREX results may provide the means to constrain K_{sym}. This is relevant given that earlier studies have suggested that the properties of finite nuclei with a relatively modest neutron-proton asymmetry are insensitive to K_{sym} [27–29].

We begin by displaying in Fig. 1(a) the well-known correlation between L and the neutron skin thickness of ^{208}Pb. For this work we employ the entire set of models used in the CREX analysis, which includes a fairly comprehensive set of covariant energy density functionals (blue dots) and a limited set of nonrelativistic skyrme models (red dots). Predictions are also included for three new covariant EDFs labeled as "DINOa-c" (colored stars) that are introduced below and in Table VI. In both Figs. 1 and 2 we display 1σ theoretical error bands obtained by including only the covariant EDFs displayed by the blue dots. Although the correlation between L and the neutron skin thickness of ^{48}Ca was anticipated not to be as robust as in the case of ^{208}Pb, Fig. 1(b) suggests that
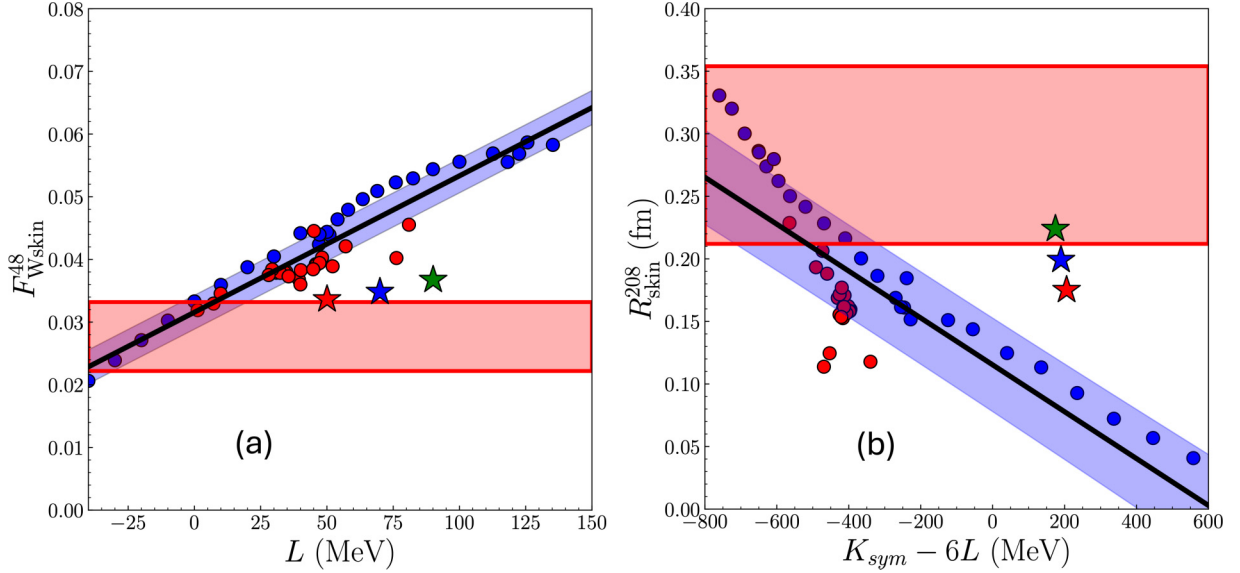
FIG. 2. (a) Model predictions for the weak skin form factor of ^{48}Ca as a function of L and (b) for the neutron skin thickness of ^{208}Pb as a function of the linear combination $K_{\text{sym}} - 6L$. The blue and red dots represent the entire set of both covariant and nonrelativistic EDFs used in the CREX analysis [1]. The new DINOa-c interactions are shown as stars, see Fig. 1. The experimental values are shown as horizontal bands, and our linear fits with 1σ errors are shown as solid lines with a blue band.

for the entire set of covariant EDFs, a very strong correlation emerges between $K_{\text{sym}} - 6L$ and the CREX weak skin form factor F_{Wskin}^{48} evaluated at the average momentum transfer of the experiment $q = 0.8733 \, \text{fm}^{-1}$.

This figure suggests— for the set of covariant EDFs employed in this work—the CREX form factor may best be correlated with linear combinations of the symmetry energy parameters. In particular, the quantity $K_{\text{sym}} - 6L$ appears in the incompressibility coefficient of asymmetric matter $K(\alpha) = K_0 + K_\tau \alpha^2 + \cdots$, where

$$K_\tau = K_{\text{sym}} - 6L - \frac{Q_0}{K_0}L. \qquad (2)$$

Here $\alpha = (N-Z)/A$, K_0 is the incompressibility coefficient of symmetric nuclear matter, and Q_0 the corresponding skewness parameter [30]. Note that although motivated by the incompressibility of asymmetric matter, we find that F_{Wskin}^{48} is slightly better correlated to $K_{\text{sym}} - 6L$ than to K_τ because of the small model dependency coming from the third term. We also note that whereas the correlation with the covariant EDFs is very sharp, the nonrelativistic models do not follow the same trend. However, the collection of nonrelativistic EDFs used here is not representative, as it spans a fairly narrow range in $K_{\text{sym}} - 6L$. Hence, investigating whether this correlation develops as one includes a comprehensive set of nonrelativistic models is warranted.

As already mentioned and now displayed in Fig. 2, neither the correlation between F_{Wskin}^{48} and L nor the correlation between R_{skin}^{208} and $K_{\text{sym}} - 6L$ is as strong as those displayed in Fig. 1. Nevertheless, we show this behavior to clarify some of the details of the statistical inference that will be implemented later on.

III. BAYESIAN INFERENCE OF L AND K_{sym}

Although we caution against the universality of the correlation between F_{Wskin}^{48} and $K_{\text{sym}} - 6L$, we nevertheless proceed to constrain both L and K_{sym} using the PREX-2 and CREX results. To account for a possible model dependence, we consider two different scenarios. In scenario 1 we determine L from PREX-2 and then use the newly found correlation between F_{Wskin}^{48} and $K_{\text{sym}} - 6L$ to extract K_{sym}. In this scenario only the set of covariant EDFs is used together with the correlations identified in Fig. 1. In scenario 2 we now add the limited set of skyrme forces together with the correlations displayed in Fig. 2. Under this scenario, which greatly increases the model uncertainty, the 1σ theoretical error bands are now expanded to include both nonrelativistic and covariant EDFs. We underscore that such analysis should be repeated using a larger set of skyrme EDFs, given that the limited set included here spans a narrow range of values for $K_{\text{sym}} - 6L$.

For our calculation of optimal L and K_{sym} values, we employ the use of a χ^2 minimization routine. The χ^2 takes into account the experimental values and the linear fits shown in Figs. 1 and 2. For the experimental errors, we use the results of the main PREX-2 [4] and CREX [1] papers. We construct our χ^2 using the standard form,

$$\chi^2 = \sum \frac{(y_i - \hat{y}_i(L, K_{\text{sym}}))^2}{\sigma_{\text{th}}^2 + \sigma_{\text{exp}}^2}, \qquad (3)$$

which we minimize using downhill simplex method [31]. Here y_i is a set of experimental observables, whose theoretical predictions $\hat{y}_i(L, K_{\text{sym}})$ are sensitive to the symmetry energy parameters L and K_{sym}, whereas σ_{th} and σ_{exp} indicate 1σ theoretical and experimental errors, respectively.

The list of models we employ in calculating our linear correlations comes directly from the main CREX paper [1],

TABLE I. List of all relativistic energy density functional (EDF) models used in the CREX analysis. Note there are several FSUGold2 and IU-δ models with different values of the slope parameter of the symmetry energy L. Also listed are $R_{\text{skin}}^{208} = R_n - R_p$ for ^{208}Pb and $F_{\text{Wskin}}^{48} = F_{ch} - F_{wk}$ for ^{48}Ca.

Model	L (MeV)	K_{sym} (MeV)	F_{Wskin}^{48}	R_{skin}^{208} (fm)
FSUGarnet [32]	50.97	59.45	0.0439	0.1611
FSUGold2 [33]	112.68	25.38	0.0568	0.2863
FSUGold2 (47) [34]	47.0	53.98	0.0424	0.1517
FSUGold2 (50) [34]	50.0	30.23	0.0444	0.1688
FSUGold2 (54) [34]	54.0	3.67	0.0464	0.1864
FSUGold2 (58) [34]	58.0	−17.8	0.0479	0.2004
FSUGold2 (69) [34]	69.0	−54.97	0.0509	0.2284
FSUGold2 (76) [34]	76.0	−64.40	0.0523	0.2416
FSUGold2 (90) [34]	90.0	−55.47	0.0544	0.2623
FSUGold2 (100) [34]	100.0	−29.14	0.0556	0.2740
IUFSU [35]	47.21	28.53	0.044	0.1615
NL3 [36]	118.2	100.88	0.0555	0.2798
RMF022 [32]	63.52	−28.76	0.0496	0.2164
RMF028 [32]	112.65	26.26	0.0569	0.2851
RMF032 [32]	125.63	28.68	0.0587	0.3201
TAMUa [37]	82.49	−68.37	0.0529	0.2502
TAMUb [37]	122.53	45.88	0.0569	0.3002
TAMUc [37]	135.25	51.64	0.0583	0.3306
IUδ (−40) [1]	−40.0	318	0.0206	0.0408
IUδ (−30) [1]	−30.0	266	0.0239	0.0568
IUδ (−20) [1]	−20.0	217	0.0271	0.0722
IUδ (−10) [1]	−10.0	175	0.0302	0.0928
IUδ (0) [1]	0.0	135	0.0333	0.1133
IUδ (10) [1]	10.0	100	0.0359	0.1247
IUδ (20) [1]	20.0	65	0.0388	0.1438
IUδ (30) [1]	30.0	56	0.0405	0.1510
IUδ (40) [1]	40.0	1.0	0.0442	0.1846

TABLE II. List of all nonrelativistic EDF models used in the CREX analysis, similar to Table I.

Model	L (MeV)	K_{sym} (MeV)	F_{Wskin}^{48}	R_{skin}^{208} (fm)
SI [38]	1.22	−461.85	0.0319	0.1138
SIII [39]	9.91	−393.74	0.0345	0.1246
SKM* [40]	45.78	−155.94	0.0392	0.1688
SLy4 [41]	45.96	−119.7	0.0391	0.1596
SLy5 [42]	48.14	−112.76	0.0403	0.1622
SLy7 [42]	47.22	−113.32	0.0394	0.1583
SV-K218 [43]	34.62	−206.88	0.0381	0.1622
SV-K226 [43]	34.09	−211.92	0.0379	0.1599
SV-K241 [43]	30.95	−230.77	0.0379	0.1527
SV-bas [43]	32.36	−221.76	0.0379	0.1559
SV-kap00 [43]	39.44	−161.78	0.0368	0.158
SV-kap02 [43]	35.54	−193.2	0.0373	0.1565
SV-kap06 [43]	29.33	−249.76	0.0384	0.1555
SV-mas07 [43]	52.15	−98.77	0.0389	0.1708
SV-mas08 [43]	40.15	−172.39	0.0383	0.1616
SV-mas10 [43]	28.03	−252.51	0.0375	0.1536
SV-sym28 [43]	7.21	−296.51	0.033	0.1178
SV-sym32 [43]	57.07	−148.8	0.0421	0.1933
SV-sym34 [43]	80.95	−79.08	0.0455	0.2287
SV-min [43]	44.81	−156.57	0.0384	0.1716
TOV-min [44]	76.23	−15.62	0.0402	0.2064
UNEDF0 [45]	45.08	−189.68	0.0445	0.1882
UNEDF1 [46]	40.00	−179.48	0.036	0.177

given in Tables I and II. Important for our determination of both parameters is the model uncertainty σ_{th} used in χ^2. To do this we calculate the 1σ prediction interval (PI) from the linear regression line. At each point along the regression line, the 1σ PI is calculated using

$$\sigma_{\text{th}} = t_{68\%} \times \sqrt{\frac{\sum_{i=1}^{n} (y_i - \hat{y}(x_i))^2}{n - 2}}, \qquad (4)$$

where $t_{68\%}$ is the critical t value at 68% confidence, and the terms in the square root represent the standard deviation of the residuals. The prediction interval gives us an approximate spread of values around the regression line, which indicates the region where $\sim$68% of all models should fall. For the scenario-1 fit, we fit the regression line to the covariant models only for the relations in Ref. [1]. For the scenario-2 fit, we use the regression line fit to both covariant and the skyrme models.

Once optimal values are found from the simplex method, the posterior distribution is found by maximizing the likelihood function, defined as $\mathcal{L} = \exp\left(-\frac{1}{2}\chi^2\right)$, using a Markov chain Monte Carlo approach [47]. We use a uniform prior on this approach for L in the range of $0 < L < 200$ MeV

and leave K_{sym} unconstrained. Of importance here is to note that the model error is interpolated over the x coordinate by taking half the difference of the upper and lower PI bound at each point along the regression line. Once the posterior distribution is sampled, one obtains a distribution of model parameters from which averages and standard deviations may be computed. Our results for both scenarios can be found in Table III with confidence ellipses shown in Fig. 3.

Our results paint an interesting picture of the density dependence of the symmetry energy. First, the value of $L = 110 \pm 40$ MeV extracted from scenario 1 is entirely consistent with our original published value of $L = 106 \pm 37$ MeV [25], that is also displayed in the figure. The small differences are attributed to the larger set of covariant EDFs used here. In contrast, scenario 2 favors a considerably smaller value of $L \approx 19 \pm 19$ MeV. Such a smaller value is driven by the small experimental error in F_{Wskin}^{48} relative to F_{Wskin}^{208}. So even if the correlation to L is weaker for the former than for the latter, the smaller experimental error generates the significantly smaller value of L.

TABLE III. Averages and standard deviations for the two scenarios discussed in the text.

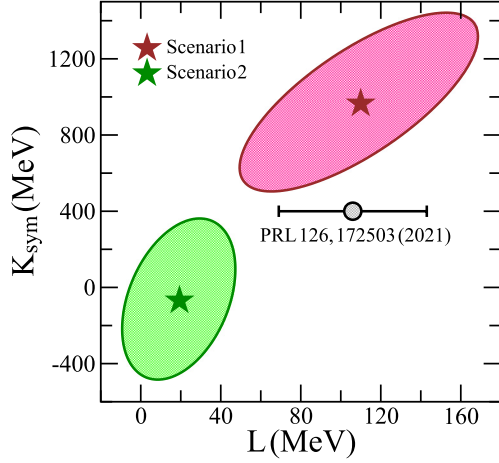| Fit	L (MeV)	K_{sym} (MeV)
Scenario 1	110 ± 40	970 ± 320
Scenario 2	19 ± 19	-61 ± 280

FIG. 3. Confidence ellipses for L and K_{sym} from Table III. We show the central values of each fit as a star, with the surrounding ellipse indicating the 67% confidence interval. Notably, the scenario-1 and scenario-2 fits do not overlap. We also show the constraint on L from [25].

Whereas our knowledge of L has improved since the culmination of the PREX campaigns, K_{sym} has remained largely unconstrained, with an overwhelming number of theoretical approaches favoring negative values. In contrast, scenario 1 favors positive values for K_{sym} at the 3σ level. It is only by including the limited set of nonrelativistic models, in combination with the small values of L, that K_{sym} is allowed to take negative values. We find this possible conflict particularly interesting. After all, one of the main motivations behind CREX was the use of *ab initio* models to inform and improve the isovector sector of energy density functionals [15].

IV. NEWLY CREATED COVARIANT MODEL SET

However, before incorporating *ab initio* predictions, we adopt the scenario-1 PREX-2–CREX constraints in an attempt to generate three new covariant EDFs with large and positive values for K_{sym}. These models, named "DINOa,b,c," are members of the "FSUGold" class of covariant EDFs [9,48] but with a notable addition to the isovector sector. In the past, the isovector sector of this class of models included only two terms: a Yukawa coupling of the nucleon to the isovector ρ meson and a nonlinear ω-ρ isoscalar-isovector cross-coupling term. In this work we add a contribution to the isovector sector arising from the Yukawa coupling of the nucleon to the scalar-isovector δ meson [49–54]. The presence of the δ meson splits the nucleon effective mass, thereby providing an

additional degree of freedom in selecting K_{sym}. To span the range of reasonable values for L, we have defined the DINOa, DINOb, and DINOc models by fixing the slope of the symmetry energy at $L = 50, 70, 90$ MeV, respectively. Our fitting procedure follows closely that of Ref. [35], supplemented by the inclusion of both R_{skin}^{208} and F_{Wskin}^{48} into the calibration.

We begin our construction with the class of FSUGold-like models featuring the δ meson [48,55]. The interaction Lagrangian for this class of models is

$$\mathcal{L}_{int} = \bar{\psi}[\mathcal{S}(\phi, \boldsymbol{\delta}) - \mathcal{V}_\mu(V_\mu, \boldsymbol{b_\mu}, A_\mu)\gamma^\mu]\psi - U(\phi)$$
$$+ \frac{\zeta}{4!}g_v^4(V_\mu V^\mu)^2 + \Lambda_v g_v^2 g_\rho^2 V_\mu V^\mu \boldsymbol{b_\mu} \cdot \boldsymbol{b^\mu}, \quad (5)$$

where

$$\mathcal{S}(\phi, \boldsymbol{\delta}) = g_s\phi + \frac{g_\delta}{2}\boldsymbol{\tau} \cdot \boldsymbol{\delta}$$

$$\mathcal{V}_\mu(V_\mu, \boldsymbol{b_\mu}, A_\mu) = g_vV_\mu + \frac{g_\rho}{2}\boldsymbol{\tau} \cdot \boldsymbol{b_\mu} + \frac{e}{2}(1 + \tau_3)A_\mu$$

$$U(\phi) = \frac{\kappa}{3!}(g_s\phi)^3 + \frac{\lambda}{4!}(g_s\phi)^4. \quad (6)$$

This class of models contains the interactions of nucleons (ψ) via the exchange of the scalar σ (ϕ) and vector ω (V_μ) mesons as well as the vector-isovector ρ meson ($\boldsymbol{b^\mu}$) and, in this work, the additional vector-isoscalar δ meson ($\boldsymbol{\delta}$). In addition to interactions among the nucleons, this Lagrangian class also includes many self- and cross-coupling terms. These are κ and λ for the cubic and quartic scalar self-coupling, ζ for the quartic ω self-coupling, and Λ_v as the ω-ρ cross coupling.

Motivated by our findings of large positive K_{sym} value from the scenario-1 fit, we choose to generate three models, which we expect fully explore the parameter space. The generation of new models follows a similar prescription as described in Ref. [56], which we summarize here briefly. For each model we fix the value of the symmetry energy at subsaturation density $k_F = 1.15$ fm^{-1} to be $\tilde{J} = 27$ MeV. This value has been shown to agree well with measurements of nuclear masses. We then fix L for the three models at 50, 70, and 90 MeV to give a good range of L values favored from multiple sources, including PREX-2. We also fix the ζ parameter to 0.015, which controls the high-density components of the EOS. This allows our models to predict neutron star masses consistent with the most recent observational and theoretical constraints on the maximum mass [57–62]. From here we take a typical set of bulk nuclear matter properties and adjust the isoscalar bulk properties to fit the binding energy and charge radii (with spin-orbit corrections [63]) of ^{40}Ca, ^{48}Ca, and ^{208}Pb.

The inversion of bulk properties to relativistic mean-field (RMF) Lagrangian couplings has been described in Ref. [33].

TABLE IV. Coupling constants of the DINO set of models. For each of the three models, we fix $m_v = 782.5$ MeV, $m_\rho = 763$ MeV, and $m_\delta = 980$ MeV as well as the quartic vector self-coupling $\zeta = 0.015$. Scalar meson mass and nonlinear κ values given in MeV.

Model	m_s	g_s^2	g_δ^2	g_v^2	g_ρ^2	κ	λ	ζ	Λ_v
DINOa	490.050	93.9422	1115.15	154.436	805.891	4.9860	−0.01370	0.015	0.0016497
DINOb	485.795	91.0316	1252.71	150.824	877.121	5.2914	−0.01488	0.015	0.0014014
DINOc	484.162	90.6481	1343.25	151.048	922.617	5.3209	−0.01497	0.015	0.0012312

TABLE V. Bulk properties of nuclear matter for our set of DINO models. Tilde denotes symmetry energy values taken at subsaturation density ($\tilde{k}_F = 1.15\,\text{fm}^{-1}$). Here $K(\alpha)$ is calculated using the Eq. (18c) of [30] for $\alpha = (126 - 82)/208$.

Model	ρ_0 (fm^{-3})	ϵ_0 (MeV)	K_0 (MeV)	Q_0 (MeV)	$\tilde{J}$ (MeV)	J (MeV)	L (MeV)	K_{sym} (MeV)	K_τ (MeV)	$K(\alpha)$ (MeV)
DINOa	0.1522	-16.16	210.0	-361.4	27.00	31.42	50.00	506.0	292.1	223.1
DINOb	0.1525	-16.21	207.0	-412.0	27.00	33.07	70.00	610.0	329.3	221.7
DINOc	0.1519	-16.22	206.0	-426.1	27.00	34.58	90.00	715.0	361.2	222.2

It was found that the giant monopole resonances (GMRs) are sensitive primarily to the incompressibility of neutron-rich matter, $K(\alpha)$ [64]. In our previous work [37] we found that for ^{208}Pb this corresponds to $K(\alpha) \approx 222$ MeV for the RMF parametrizations that yield consistent GMRs. Hence we applied this constraint to $K(\alpha)$ in the DINO models. All that is left now is to pick a value for K_{sym} which minimizes the squared difference of R_{skin}^{208} and F_{Wskin}^{48} from their experimental values. The differences between the model predictions and experimental results for each observable are then used to generate a new set of parameters until a parameter set converges.

It should be noted that a direct inversion of couplings from $\tilde{J}$, L, and K_{sym} does not presently exist, as the presence of the additional δ meson introduces much more complexity than has previously been detailed. As such, we use a downhill simplex routine to determine the isovector couplings g_ρ^2, g_δ^2, and Λ_v. Furthermore, there exist some combinations of bulk nuclear properties that do not produce a convergent set of parameters, which requires careful calculation schemes.

The coupling constants of the three DINO models can be found in Table IV. We find that due to the large value of K_{sym}, the isovector Yukawa couplings g_ρ^2 and g_δ^2 are very large. Additionally, we report the bulk parameters of the nuclear EOS in Table V as predicted by these three models. In the next section, using this new parameter set we proceed to calculate the properties of finite nuclei and neutron stars.

V. DINO MODEL PREDICTIONS

A. Predictions of nuclei

We start this section by mentioning that the new model parameters, together with predictions for the bulk properties of infinite nuclear matter, are given in Tables IV and V, respectively. It is worth mentioning, however, that in all three cases,

the curvature of the symmetry energy is large and positive, namely, $K_{\text{sym}} = 506$, 610, and 715 MeV for DINOa, DINOb, and DINOc, respectively. Regardless, we find that the results for the binding energy, charge radii, and form factors of ^{48}Ca and ^{208}Pb as listed in Table VI are all in good agreement with the experiment. In the particular case of F_{Wskin}^{208} and F_{Wskin}^{48}, predictions for the large set of models considered here alongside the predictions from the three DINO models are displayed in Fig. 4. This figure highlights the predicament faced by most energy density functionals: with few exceptions, most models fall outside the 90% confidence ellipse. In this sense the three DINO models do quite well compared to the other models considered.

However, the DINO models' large isovector couplings do begin to introduce anomalies in the point particle densities. In particular, the proton and neutron densities in the core of both ^{48}Ca and ^{208}Pb show large density fluctuations that are nonphysical, see Figs. 5 and 6. For example, ^{208}Pb is a heavy closed-shell nucleus, and so we expect the nucleus to saturate at a density value near ρ_0 [12,69]. For the DINO models, ^{208}Pb has very large fluctuations and *does not* saturate. This anomaly is largely due to the isovector g_δ^2 coupling splitting the proton and neutron masses, thereby causing a larger proton density in the core and a small neutron density. We see similar fluctuations in ^{48}Ca, although the saturation property is less strict for lighter nuclei.

B. Predictions of neutron star properties

Our calculation of neutron star (NS) structure begins by following the standard practices of relativistic mean-field theory to calculate the equation of state of the core [55,70,71]. This includes calculating the pressure and energy density of protons, neutrons, electrons, and muons in beta equilibrium using the interaction Lagrangian of Eq. (6). The outer

TABLE VI. Experimental data for the binding energy per nucleon (in MeV) [65], charge radii (in fm) [66], neutron skins, and form factor skins [1,4] for ^{48}Ca and ^{208}Pb nuclei used in the optimization. Also displayed are the theoretical results obtained with IUFSU [35], FSUGold2 [67], BigApple [68], and the three new parametrizations.

| Nucleus	Observable	Experiment	IUFSU	FSUGold2	BigApple	DINOa	DINOb	DINOc
^{48}Ca	B/A (MeV)	8.667	8.549	8.621	8.531	8.670	8.667	8.667
	R_{ch} (fm)	3.477 ± 0.002	3.416	3.413	3.447	3.454	3.458	3.461
	R_{skin} (fm)	0.121 ± 0.035	0.1731	0.2319	0.1682	0.0996	0.1051	0.1135
	F_{Wskin} (q_{CREX})	0.0277 ± 0.0055	0.0439	0.0568	0.0417	0.0333	0.0349	0.0367
^{208}Pb	B/A (MeV)	7.867	7.896	7.872	7.872	7.867	7.867	7.867
	R_{ch} (fm)	5.501 ± 0.001	5.476	5.489	5.490	5.502	5.503	5.503
	R_{skin} (fm)	0.283 ± 0.071	0.1615	0.2863	0.1506	0.1748	0.1993	0.2240
	F_{Wskin} (q_{PREX})	0.041 ± 0.013	0.0233	0.0423	0.0215	0.0263	0.0303	0.0344
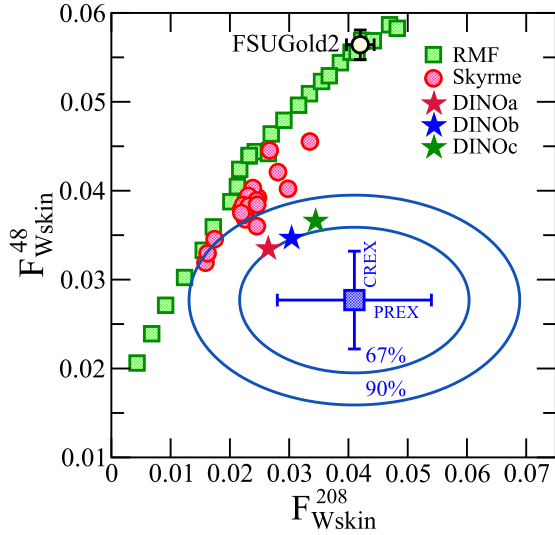
FIG. 4. Predictions for the weak skin form factor of ^{208}Pb and ^{48}Ca for the entire set of covariant RMF (green squares) and nonrelativistic skyrme (pink circles) EDFs considered in this paper. The blue ellipses represent joint PREX-2 and CREX 67% and 90% probability contours, respectively, just as in Fig. 2 of Ref. [1]. The FSUGold2 prediction is included to illustrate typical statistical uncertainties. Depicted with stars are the prediction of the three new DINO models.

crust is tabulated using the mass table of Duflo and Zuker [72] up to neutron drip $\sim 10^{-4}$ fm^{-3}. The outer crust and core equations of state are then interpolated using a cubic polynomial, ensuring both the density and sound speed are continuous at each interface as in Ref. [11]. We should note that the prescription for the inner crust may account for as much as a 0.5-km difference, depending on the formalism used. However, the tidal deformability is insensitive to the crust EOS [11]. The inner crust-core transition density is determined using the RPA dynamical method [10,73], with

FIG. 6. Point neutron (solid) and proton (dashed) densities in ^{48}Ca for the DINO family of models.

a slight modification to accompany the presence of the δ meson [74].

Although the DINO models are consistent with the properties of finite nuclei (see Table VI), their large values for K_{sym} induce a dramatic stiffening of the EOS at the high densities of relevance to neutron stars. Such a stiffening generates neutron star radii that are too large when compared against LIGO-Virgo and NICER data. This behavior is illustrated in Fig. 7, with explicit values in Table VII, which displays the so-called "Holy Grail" of neutron star physics: the mass-radius relation. Together with the predictions from the three DINO models and a few other covariant EDFs, the figure shows mass-radius determinations by the NICER mission for the two pulsars PSR J0030+045 [75,76] and PSR J0740+6620 [60,61].

With radii of about 15 km, the predictions from all three DINO models are inconsistent with the NICER data for the

FIG. 5. Point neutron (solid) and proton (dashed) densities in ^{208}Pb for the DINO family of models. Note that the central proton density for DINOc is shown off the plot.
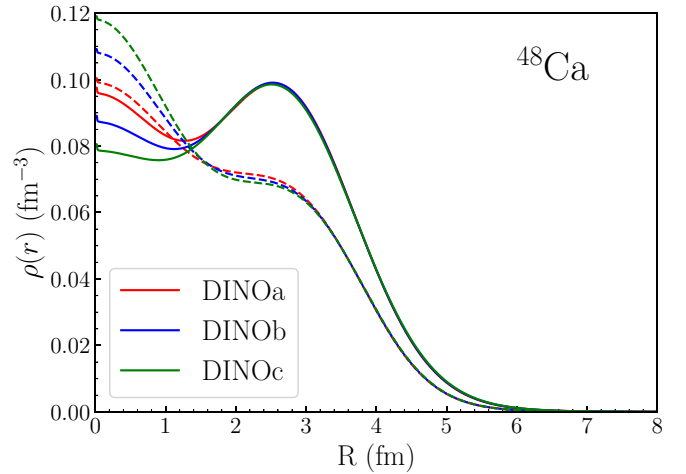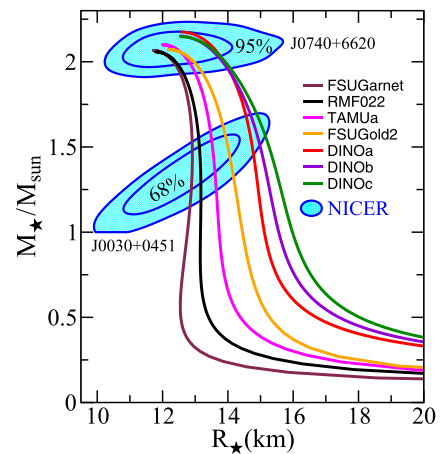

FIG. 7. Mass-radius relation for neutron stars. Along with our three DINO models, predictions are also shown for a few covariant energy density functionals. The two sets of contours display the NICER mass-radius constraints of two pulsars, PSR J0030+0451 [75,76] and PSR J0740+6620 [60,61], at 68% and 95% confidence, respectively.

TABLE VII. Prediction of various neutron star observables for our models. We calculate the core-crust transition density as described in Ref. [10], with the modification to account for the addition of δ mesons.

Model	M_{max} ($M_\odot$)	$R_{1.4}$ (km)	$\Lambda_{1.4}$	ρ_t (fm^{-3})	ρ_{Urca} (fm^{-3})	M_{Urca} ($M_\odot$)
DINOa	2.17	14.82	1050.6	0.0914	0.1580	0.418
DINOb	2.15	15.11	1128.2	0.0846	0.1438	0.427
DINOc	2.14	15.41	1240.4	0.0789	0.1373	0.458

low-mass star. With such large radii, the models also predict very large tidal deformabilities that are highly disfavored by GW170817 [77–81]. In particular, we find that DINO models predict larger neutron star radii and lower densities for the direct Urca threshold. To agree with radii observation, one expects that a phase transition or other strong density dependence develops at intermediate densities. Moreover, a very small density for the direct Urca threshold suggests that all neutron stars with normal matter would undergo fast cooling, which does not agree with the cooling observations [82]. If these predictions stand true, it raises the intriguing possibility of a neutron star core permeated with superfluid or superconductive matter throughout. Or in conjunction with the radii observation, this may even imply the prospect of an earlier onset of a phase transition to exotic states. Hence we must conclude that while the DINO models provide a plausible solution to the PREX-2–CREX dilemma, they fail to reproduce astrophysical observations—unless a phase transition or other strong density dependence develops at intermediate densities. The emergence of a phase transition—normally accompanied by a softening of the EOS—has been shown to reduce the radius and deformability of neutron stars [83–85].

VI. CONCLUSIONS

In conclusion, the recently measured weak skin form factor in ^{48}Ca by the CREX Collaboration paints a peculiar picture for the behavior of neutron-rich matter. When combined with the PREX-2 result that favors a large value for L, the newly revealed correlation between F_{Wskin}^{48} and the combination of bulk symmetry energy parameters $K_{sym} - 6L$ motivates the calibration of a new set of covariant EDFs with large and

positive values for K_{sym}. This result is in striking contrast to most nonrelativistic EDFs and *ab initio* models that instead predict negative values for K_{sym}. Nevertheless, the newly created DINO models with such unconventional values for K_{sym} agree better with PREX and CREX than many EDFs existent in the literature. However, this accomplishment comes at the price of stiffening the equation of state at the high densities of relevance to neutron stars, resulting in a failure to accommodate the recent NICER constraints. Nonetheless, these models represent a first step in reconciling PREX and CREX for covariant EDFs.

Moving forward, the Mainz Radius Experiment (MREX) at the future Mainz Energy-Recovery Superconducting Accelerator (MESA) [86] promises to increase the precision of R_{skin}^{208} by a factor of 2. MREX will then confirm whether the slope of the symmetry energy is indeed stif or if the PREX-2 measurement represents a large statistical fluctuation. Further, that most theoretical models disfavor large and positive values for K_{sym} may suggest that the strong correlation uncovered here may be model dependent. Should this be the case, then *ab initio* models could inform how to improve the isovector sector of energy density functionals [15]. Finally, although the stiff symmetry energy suggested by the DINO models at high densities are ruled out by observation, these models could still be fruitful in describing the properties of atomic nuclei—especially if a phase transition emerges at intermediate densities. Regardless, the PREX-2–CREX tension continues to reenergize the theoretical, experimental, and observational communities in our common quest to understand the behavior of dense, neutron-rich matter.

ACKNOWLEDGMENTS

[1] D. Adhikari *et al.* (CREX Collaboration), Phys. Rev. Lett. **129**, 042501 (2022).

[2] S. Abrahamyan *et al.* (PREX Collaboration), Phys. Rev. Lett. **108**, 112502 (2012).

[3] C. J. Horowitz, Z. Ahmed, C. M. Jen, A. Rakhman, P. A. Souder, M. M. Dalton, N. Liyanage, K. D. Paschke, K. Saenboonruang, R. Silwal, G. B. Franklin, M. Friend, B. Quinn, K. S. Kumar, D. McNulty, L. Mercado, S. Riordan, J. Wexler, R. W. Michaels, and G. M. Urciuoli, Phys. Rev. C **85**, 032501(R) (2012).

[4] D. Adhikari *et al.* (PREX Collaboration), Phys. Rev. Lett. **126**, 172502 (2021).

[5] B. A. Brown, Phys. Rev. Lett. **85**, 5296 (2000).

[6] R. J. Furnstahl, Nucl. Phys. A **706**, 85 (2002).

[7] X. Roca-Maza, M. Centelles, X. Viñas, and M. Warda, Phys. Rev. Lett. **106**, 252501 (2011).

[8] C. J. Horowitz and J. Piekarewicz, Phys. Rev. Lett. **86**, 5647 (2001).

[9] C. J. Horowitz and J. Piekarewicz, Phys. Rev. C **64**, 062802(R) (2001).

[10] J. Carriere, C. J. Horowitz, and J. Piekarewicz, Astrophys. J. **593**, 463 (2003).

[11] J. Piekarewicz and F. J. Fattoyev, Phys. Today **72**(7), 30 (2019).

[12] H. De Vries, C. W. De Jager, and C. De Vries, At. Data Nucl. Data Tables **36**, 495 (1987).

[13] M. Thiel, C. Sfienti, J. Piekarewicz, C. J. Horowitz, and M. Vanderhaeghen, J. Phys. G **46**, 093003 (2019).

[14] C. J. Horowitz and J. Piekarewicz, Phys. Rev. C **86**, 045503 (2012).

[15] S. Riordan *et al.*, CREX: Parity-violating measurement of the weak charge distribution of ^{48}Ca to 0.02 fm accuracy, JLAB-PR-40-12-004, TJNAF (2013), http://hallaweb.jlab.org/parity/prex/c-rex2013_v7.pdf.

[16] J. Piekarewicz, B. K. Agrawal, G. Colò, W. Nazarewicz, N. Paar, P. G. Reinhard, X. Roca-Maza, and D. Vretenar, Phys. Rev. C **85**, 041302(R) (2012).

[17] B. Hu *et al.*, Nat. Phys. **18**, 1196 (2022).

[18] P.-G. Reinhard, X. Roca-Maza, and W. Nazarewicz, Phys. Rev. Lett. **129**, 232501 (2022).

[19] Z. Zhang and L.-W. Chen, Phys. Rev. C **108**, 024317 (2023).

[20] C. Mondal and F. Gulminelli, Phys. Rev. C **107**, 015801 (2023).

[21] P. Papakonstantinou, arXiv:2210.02696.

[22] E. Yüksel and N. Paar, Phys. Lett. B **836**, 137622 (2023).

[23] F. Sammarruca, Symmetry **16**, 34 (2024).

[24] G. Hagen *et al.*, Nat. Phys. **12**, 186 (2016).

[25] B. T. Reed, F. J. Fattoyev, C. J. Horowitz, and J. Piekarewicz, Phys. Rev. Lett. **126**, 172503 (2021).

[26] P. Papakonstantinou, arXiv:2210.02696.

[27] M. B. Tsang, Y. Zhang, P. Danielewicz, M. Famiano, Z. Li, W. G. Lynch, and A. W. Steiner, Phys. Rev. Lett. **102**, 122701 (2009).

[28] M. B. Tsang, J. R. Stone, F. Camera, P. Danielewicz, S. Gandolfi, K. Hebeler, C. J. Horowitz, J. Lee, W. G. Lynch, Z. Kohley, R. Lemmon, P. Moller, T. Murakami, S. Riordan, X. Roca-Maza, F. Sammarruca, A. W. Steiner, I. Vidana, and S. J. Yennello, Phys. Rev. C **86**, 015803 (2012).

[29] P. Danielewicz, P. Singh, and J. Lee, Nucl. Phys. A **958**, 147 (2017).

[30] J. Piekarewicz and M. Centelles, Phys. Rev. C **79**, 054311 (2009).

[31] P. Virtanen, R. Gommers, T. E. Oliphant, M. Haberland, T. Reddy, D. Cournapeau, E. Burovski, P. Peterson, W. Weckesser, J. Bright *et al.*, Nat. Methods **17**, 261 (2020).

[32] W.-C. Chen and J. Piekarewicz, Phys. Rev. Lett. **115**, 161101 (2015).

[33] W.-C. Chen and J. Piekarewicz, Phys. Lett. B **748**, 284 (2015).

[34] F. J. Fattoyev, J. Piekarewicz, and C. J. Horowitz, Phys. Rev. Lett. **120**, 172702 (2018).

[35] F. J. Fattoyev, C. J. Horowitz, J. Piekarewicz, and G. Shen, Phys. Rev. C **82**, 055803 (2010).

[36] G. A. Lalazissis, J. Konig, and P. Ring, Phys. Rev. C **55**, 540 (1997).

[37] F. J. Fattoyev and J. Piekarewicz, Phys. Rev. Lett. **111**, 162501 (2013).

[38] T. H. R. Skyrme, Philos. Mag. **1**, 1043 (1956).

[39] D. Vautherin and D. M. Brink, Phys. Rev. C **5**, 626 (1972).

[40] J. Bartel, P. Quentin, M. Brack, C. Guet, and H.-B. Håkansson, Nucl. Phys. A **386**, 79 (1982).

[41] E. Chabanat, P. Bonche, P. Haensel, J. Meyer, and R. Schaeffer, Nucl. Phys. A **635**, 231 (1998).

[42] P.-G. Reinhard, D. J. Dean, W. Nazarewicz, J. Dobaczewski, J. A. Maruhn, and M. R. Strayer, Phys. Rev. C **60**, 014316 (1999).

[43] P. Klupfel, P.-G. Reinhard, T. J. Burvenich, and J. A. Maruhn, Phys. Rev. C **79**, 034310 (2009).

[44] J. Erler, C. J. Horowitz, W. Nazarewicz, M. Rafalski, and P.-G. Reinhard, Phys. Rev. C **87**, 044320 (2013).

[45] M. Kortelainen, R. J. Furnstahl, W. Nazarewicz, and M. V. Stoitsov, Phys. Rev. C **82**, 011304(R) (2010).

[46] M. Kortelainen, T. Lesinski, J. More, W. Nazarewicz, J. Sarich, N. Schunck, M. V. Stoitsov, and S. Wild, Phys. Rev. C **82**, 024313 (2010).

[47] D. Foreman-Mackey, D. W. Hogg, D. Lang, and J. Goodman, Publ. Astron. Soc. Pac. **125**, 306 (2013).

[48] B. G. Todd-Rutel and J. Piekarewicz, Phys. Rev. Lett. **95**, 122501 (2005).

[49] S. Kubis, M. Kutschera, and S. Stachniewicz, Acta Phys. Polon. **B29**, 809 (1998).

[50] F. Hofmann, C. M. Keil, and H. Lenske, Phys. Rev. C **64**, 034314 (2001).

[51] B. Liu, V. Greco, V. Baran, M. Colonna, and M. Di Toro, Phys. Rev. C **65**, 045201 (2002).

[52] V. Greco, V. Baran, M. Colonna, M. Di Toro, T. Gaitanos, and H. H. Wolter, Phys. Lett. B **562**, 215 (2003).

[53] J. K. Bunta and S. Gmuca, Phys. Rev. C **68**, 054318 (2003).

[54] B. Liu, H. Guo, M. Di Toro, and V. Greco, Eur. Phys. J. A **25**, 293 (2005).

[55] S. K. Singh, S. K. Biswal, M. Bhuyan, and S. K. Patra, Phys. Rev. C **89**, 044001 (2014).

[56] F. J. Fattoyev and J. Piekarewicz, Phys. Rev. C **82**, 025805 (2010).

[57] P. Demorest, T. Pennucci, S. Ransom, M. Roberts, and J. Hessels, Nature (London) **467**, 1081 (2010).

[58] J. Antoniadis, P. C. Freire, N. Wex, T. M. Tauris, R. S. Lynch, M. H. van Kerkwijk, M. Kramer, C. Bassa, V. S. Dhillon, T. Driebe *et al.*, Science **340**, 1233232 (2013).

[59] L. Rezzolla, E. R. Most, and L. R. Weih, Astrophys. J. Lett. **852**, L25 (2018).

[60] M. C. Miller *et al.*, Astrophys. J. Lett. **918**, L28 (2021).

[61] T. E. Riley *et al.*, Astrophys. J. Lett. **918**, L27 (2021).

[62] R. W. Romani, D. Kandel, A. V. Filippenko, T. G. Brink, and W. Zheng, Astrophys. J. Lett. **934**, L17 (2022).

[63] C. J. Horowitz and K. Kadau, Phys. Rev. Lett. **102**, 191102 (2009).

[64] J. Piekarewicz, J. Phys. G **37**, 064038 (2010).

[65] M. Wang, G. Audi, A. H. Wapstra, F. G. Kondev, M. MacCormick, X. Xu, and B. Pfeiffer, Chin. Phys. C **36**, 1603 (2012).

[66] I. Angeli and K. Marinova, At. Data Nucl. Data Tables **99**, 69 (2013).

[67] W.-C. Chen and J. Piekarewicz, Phys. Rev. C **90**, 044305 (2014).

[68] F. J. Fattoyev, C. J. Horowitz, J. Piekarewicz, and B. Reed, Phys. Rev. C **102**, 065805 (2020).

[69] C. J. Horowitz, J. Piekarewicz, and B. Reed, Phys. Rev. C **102**, 044321 (2020).

[70] N. K. Glendenning, *Compact Stars* (Springer-Verlag, New York, 2000).

[71] F. Fattoyev, Sensitivity of neutron star properties to the equation of state, Ph.D. thesis, Florida State University, 2011.

[72] J. Duflo and A. P. Zuker, Phys. Rev. C **52**, R23 (1995).

[73] G. Baym and E. Flowers, Nucl. Phys. A **222**, 29 (1974).

[74] B. T. Reed, Neutron starts and neutron skins: a crossroads in nuclear astrophysics, Ph.D. thesis, 2023, https://www.proquest.com/dissertations-theses/neutron-stars-skins-crossroads-nuclear/docview/2841238132/se-2.

[75] M. C. Miller *et al.*, Astrophys. J. Lett. **887**, L24 (2019).

[76] T. E. Riley *et al.*, Astrophys. J. Lett. **887**, L21 (2019).

[77] B. P. Abbott *et al.* (LIGO Scientific Collaboration and Virgo Collaboration), Phys. Rev. Lett. **119**, 161101 (2017).

[78] T. Malik, N. Alam, M. Fortin, C. Providencia, B. K. Agrawal, T. K. Jha, B. Kumar, and S. K. Patra, Phys. Rev. C **98**, 035804 (2018).

[79] E. R. Most, L. R. Weih, L. Rezzolla, and J. Schaffner-Bielich, Phys. Rev. Lett. **120**, 261103 (2018).

[80] D. Radice and L. Dai, Eur. Phys. J. A **55**, 50 (2019).

[81] I. Tews, J. Margueron, and S. Reddy, Phys. Rev. C **98**, 045804 (2018).

[82] M. V. Beznogov and D. G. Yakovlev, Mon. Not. Roy. Astron. Soc. **452**, 540 (2015).

[83] K. Chatziioannou, Phys. Rev. D **105**, 084021 (2022).

[84] S. Han and A. W. Steiner, Phys. Rev. D **99**, 083014 (2019).

[85] W.-J. Xie and B.-A. Li, Phys. Rev. C **103**, 035802 (2021).

[86] D. Becker, Eur. Phys. J. A **54**, 208 (2018).